INORGANIC CHEMISTRY FRONTIERS

RESEARCH ARTICLE

View Article Online
View Journal | View Issue

Cite this: *Inorg. Chem. Front.*, 2023, **10**, 2677

The β-$PdBi_2$ monolayer for efficient electrocatalytic NO reduction to NH_3: a computational study†

Yuting Sun,[a] Zhongxu Wang,[a] Yuejie Liu,*[b] Qinghai Cai [a,c] and Jingxiang Zhao *[a]

Received 6th February 2023,
Accepted 24th March 2023

DOI: 10.1039/d3qi00225j

rsc.li/frontiers-inorganic

Electrocatalytic NO reduction to NH_3 (NORR) is regarded as an appealing strategy for both sustainable NH_3 production and harmful NO abatement, but the development of highly active and selective electrocatalysts to boost such a complex multiple proton-coupled electron-transferred process still remains a challenge. Here, by means of density functional theory (DFT) computations, we proposed the synthesized β-$PdBi_2$ monolayer as a highly efficient NORR catalyst. Our results revealed that the β-$PdBi_2$ monolayer possesses outstanding thermodynamic, dynamic, and electrochemical stabilities, as well as intrinsic metallicity. In particular, this catalyst exhibits excellent catalytic activity towards NORR with a low limiting potential of −0.35 V, which can be further enhanced by applying a suitable tensile strain. In addition, we also explored the effects of pH and applied potential on NORR over the β-$PdBi_2$ monolayer, among which an alkaline environment of pH = 7.92 facilitates the effective NO-to-NH_3 conversion. Thus, the β-$PdBi_2$ monolayer can be utilized as a promising catalyst with high efficiency for NORR, which offers cost-effective opportunities for advancing sustainable NH_3 production and eliminating nitric oxide pollutants.

1. Introduction

As one of the most significant synthetic chemicals in industry, ammonia (NH_3) is not only a vital ingredient and building block of many nitrogenous compounds for the manufacture of plastics, explosives, fibers, dyes, and pharmaceuticals, but also is responsible for the production of 85% of fertilizers to boost sustainable food for meeting the ever-growing global population.[1–4] In addition, NH_3 is an ideal carbon-free H_2 fuel for energy storage and transportation due to its high hydrogen content of 17.5%.[5,6] At present, the large-scale NH_3 synthesis mainly depends on the traditional Haber–Bosch process, which has been regarded as the most impactful invention of the 20th century.[7,8] However, such a process is energy intensive in that it requires harsh conditions (*e.g.*, 400–500 °C and 150 bar) to break the highly inert N≡N triple bond, leading to mass CO_2 emissions and extensive energy consumption.[9,10] Recently, the electrocatalytic N_2-to-NH_3 conversion (NRR) under ambient conditions has emerged as a green and energy-saving alternative to the Haber–Bosch technology.[11–14] Nevertheless, the high energy (941 kJ mol^{-1}) required for N_2 dissociation, low water solubility, and a severe competing hydrogen evolution reaction (HER) make the NRR process suffer from serious activity and selectivity problems.[15–18] Thus, the electrochemical NH_3 synthesis from N_2 fixation still remains a huge challenge.

Compared with the N_2 reactant, nitric oxide (NO) is more reactive and possesses a lower dissociation energy of the N=O bond, rendering the NO reduction reaction (NORR) more feasible than NRR for NH_3 electrosynthesis thermodynamically.[19–21] Particularly, NO is one of the notorious air pollutants and poses a great threat to the ecological environment and human health.[22–24] Thus, NORR represents an appealing strategy to produce valuable NH_3 and to remedy NO pollution simultaneously.[25–32] Yet, the competitive HER still greatly limits the NORR, leading to low faradaic efficiencies (FE).[33–36] Thus, it is of great significance to explore stable and highly efficient catalysts made from Earth-abundant elements to impede the unwanted HER and to promote the NORR process simultaneously.

As a low-toxic, highly-stable, environmentally-friendly group-VA metal, bismuth (Bi) has received extensive attention in electrocatalysis such as N_2 fixation and CO_2 reduction.[37–45] More importantly, Bi has been revealed to exhibit a superior

[a]*College of Chemistry and Chemical Engineering, Key Laboratory of Photonic and Electronic Bandgap Materials, Ministry of Education, Harbin Normal University, Harbin 150025, Heilongjiang, China. E-mail: zhaojingxiang@hrbnu.edu.cn*
[b]*Modern Experiment Center, Harbin Normal University, Harbin, 150025, China. E-mail: liuyuejie@hrbnu.edu.cn*
[c]*Heilongjiang Province Collaborative Innovation Center of Cold Region Ecological Safety, Harbin 150025, China*

† Electronic supplementary information (ESI) available. See DOI: https://doi.org/10.1039/d3qi00225j

suppressing effect on the competitive HER due to its rather weak binding strength with H species,[46] which normally helps improve the selectivity towards the NO electrocatalytic reduction. However, bulk Bi materials exhibit low efficiency due to the absence of accessible active sites.[47,48] In this regard, the two-dimensional (2D) counterparts hold great promise for electrocatalytic application due to their large specific surface area to facilitate the diffusion of reactants and more exposed active sites to boost rapid charge transfer.[49,50] For example, Zhang *et al.* prepared ultrathin 2D Bi nanosheets towards efficient electrocatalytic CO_2 conversion with a FE of 86.0% for formic acid production.[51] Qiao's group reported that their synthesized Bi nanosheets can be used as a promising catalyst for NRR, which can be attributed to the sufficient exposure of edge sites.[45] However, the catalytic activity of these reported 2D Bi electrocatalysts is still unsatisfactory due to their low current density.[39,52] Thus, the further development of 2D Bi-based electrocatalysts with high selectivity and high efficiency for NH_3 synthesis from NORR is of great significance.

Herein, by means of density functional theory (DFT) computations, we proposed a novel 2D material, namely the β-$PdBi_2$ monolayer, as a promising NORR catalyst. Notably, using a Bi(111) film on Si(111) as a substrate, β-$PdBi_2$ films with various layers have been successfully synthesized in experiments.[53] Our results revealed that β-$PdBi_2$ indeed exhibits good catalytic performance toward NO electroreduction to the NH_3 product with high efficiency and high selectivity, which can be further enhanced by applying a 7% tensile strain. In addition, the alkaline conditions are also conducive to boost the NORR catalytic activity of the β-$PdBi_2$ monolayer. Thus, the β-$PdBi_2$ monolayer can be utilized as an eligible NORR catalyst for NH_3 synthesis.

2. Computational models and methods

All spin-polarized density functional theory (DFT) computations were carried out by using the Vienna *Ab Initio* Simulation Package (VASP)[54,55] with the projector-augmented-wave (PAW) method,[56,57] and a cutoff energy of 550 eV was adopted. The exchange–correlation interactions were described by the Perdew–Burke–Ernzerhof (PBE) functional[58] within the generalized gradient approximation (GGA). The convergence thresholds for energy and force were set to 10^{-5} eV and 0.01 eV $Å^{-1}$, respectively. The DFT + D3 method within the Grimme scheme[59] was used to account for the van der Waals (vdW) interactions of the reaction intermediates with the catalysts.

A 4 × 4 × 1 supercell was constructed to explore the catalytic activity of the β-$PdBi_2$ monolayer, in which a vacuum space of 20 Å in the *z*-direction was adopted to avoid the interactions between periodic images. The Brillouin zone was sampled with a Monkhorst–Pack grid of 3 × 3 × 1 for geometry optimization, while a denser *k*-mesh of 15 × 15 × 1 was used for computations of electronic properties. The hybrid functional based on the Heyd–Scuseria–Ernzerhof (HSE06) method[60,61] was adopted to compute the band structure. The *ab initio* molecular dynamics (AIMD) simulations were carried out by the *NVT* ensemble with the Nose–Hoover thermostat.[62] To evaluate the electrocatalytic performance of the NO-to-NH_3 process, the Gibbs free energy changes (ΔG) of all elementary steps along all possible reaction pathways were computed by the computational hydrogen electrode (CHE) model[63,64] and further computational details are presented in the ESI.†

3. Results and discussion

3.1. Structure, stability, and electronic property of the β-$PdBi_2$ monolayer

It has been experimentally reported that 2D β-$PdBi_2$ films can be synthesized from a single layer up to dozens of triple layers using a Bi(111) film on Si(111) as the substrate based on the molecular beam epitaxy method.[53] In Fig. 1a, we have presented the structure of the optimized β-$PdBi_2$ monolayer. Obviously, the primitive cell of the β-$PdBi_2$ monolayer is square with two Bi and one Pd atoms in one unit, in which each Pd atom is located at the center of a square prism of eight Bi atoms, resulting in the formation of a layered body-centred unit cell. Furthermore, the optimized lattice constant of β-$PdBi_2$ is computed to be 3.27 Å with the length of the Pd–Bi bond being 2.98 Å. Notably, the obtained structure and the corresponding lattice parameters of the β-$PdBi_2$ monolayer were well consistent with previous theoretical studies,[65–67] indicating the accuracy of the employed methods and models in this work. Furthermore, according to the Bader charge analysis, each Bi atom with smaller electronegativity denotes 0.22 e^- to each Pd atom, accumulating positive charges on the Bi atoms (Fig. 1b), which may be conducive not only to activate the NO reactant, but also to hinder the H^+ approaching Bi active site and the *H formation due to the electrostatic repulsion between positively charged Bi and H^+. To deeply understand the bonding feature, we computed the electron localization function (ELF) of the β-$PdBi_2$ monolayer, where a large ELF (>0.5) represents the covalent bond or core electrons, whereas a smaller ELF (<0.5) corresponds to the ionic bonds, and an ELF value of 0.5 suggests the metallic nature. It can be seen from Fig. 1c that there are obvious electron delocalizations in the whole β-$PdBi_2$ monolayer, implying strong interactions between Pd and Bi atoms in the whole framework and belonging to the robust ionic bonds, which may be beneficial for the excellent stability of the β-$PdBi_2$ monolayer.

High stability is a prerequisite for the long-term application of any catalysts. We first computed the cohesive energy (E_{coh}) of the β-$PdBi_2$ monolayer using the following equation: $E_{coh} = (E_{\beta\text{-}PdBi_2} - E_{Pd} - 2E_{Bi})/3$, where $E_{\beta\text{-}PdBi_2}$, E_{Pd}, and E_{Bi} represent the total energies of the β-$PdBi_2$ monolayer, Pd, and Bi atoms. According to this definition, the computed E_{coh} of the β-$PdBi_2$ monolayer is −3.44 eV, which is comparable to those of some synthesized 2D nanomaterials, such as Cu_2Si (−3.46 eV)[68] and germanene (−3.26 eV),[68] well consistent with previous results on its experimental synthesis.[53] To assess the thermodynamic

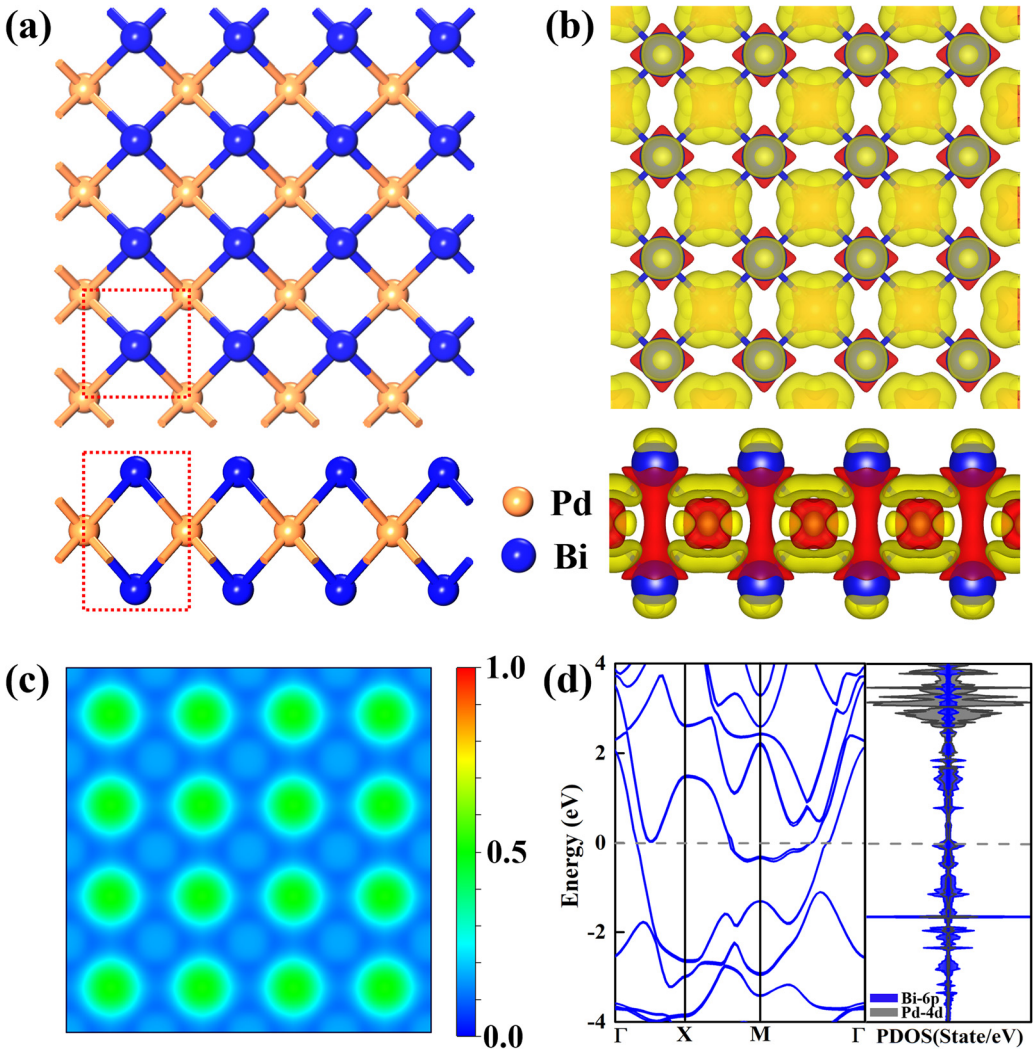

Fig. 1 (a) Top and side view of the optimized β-$PdBi_2$ monolayer. The red dashed lines represent a unit cell of the β-$PdBi_2$ monolayer. (b) The charge difference density of the β-$PdBi_2$ monolayer with an isovalue of 0.003 e $Å^{-3}$, and yellow and red bubbles represent positive and negative charges, respectively. (c) ELF analysis of β-$PdBi_2$ monolayer along the (001) plane. (d) Band structure with the spin–orbit coupling (SOC)-corrected and projected density of states (PDOS) of the β-$PdBi_2$ monolayer.

stability of the β-$PdBi_2$ monolayer, *ab initio* molecular dynamics (AIMD) simulations were further performed at 500 K. It can be observed that the β-$PdBi_2$ monolayer well maintains its pristine structure without obvious deformation throughout a 10 ps (Fig. S1 in the ESI†), indicative of its outstanding thermal stability. In addition, a good electrochemical stability is also vital to guarantee its practical application under realistic aqueous conditions. To this end, we computed the dissolution potential (U_{diss}, ESI†), which is a well-accepted descriptor to assess the electrochemical stability of a catalyst.[69,70] Fortunately, our results showed that the β-$PdBi_2$ monolayer has a positive U_{diss} of 0.75 V, suggesting that this material is electrochemically stable under realistic conditions. Another important question is whether the bare surfaces of the β-$PdBi_2$ monolayer could be covered by *O/*OH species in an aqueous solution under working conditions. To address this question, the surface Pourbaix diagram[71] of the β-$PdBi_2$ monolayer was constructed to reveal its most stable surface configurations under different equilibrium potentials and pH values. The results showed that the redox potential (U_R) of the β-$PdBi_2$ monolayer is much less negative than the corresponding U_L of NORR, indicating that this catalyst exhibits outstanding electrochemical stability against surface oxidation under working conditions (Fig. S2†).

To ensure rapid charge transfer in electrocatalysis, an excellent electrical conductivity is also indispensable. Therefore, we computed the band structure through the hybrid HSE06 functional, in which the spin–orbit coupling (SOC) effect was considered, as Bi is a heavy element. As shown in Fig. 1d, we found that there are some energy bands crossing the Fermi level, suggesting that the β-$PdBi_2$ monolayer exhibits a metallic feature. Moreover, its projected density of states (PDOSs) was computed, from which the high peaks around the Fermi level could be observed (Fig. 1d). In general, the high DOS at the

Fermi level indicates a high density of carriers, promoting good electron transfer and boosting the chemical reactivity towards the adsorbates. Thus, the β-$PdBi_2$ monolayer exhibits outstanding electrical conductivity, which may be constructive to its electrocatalytic performance. In addition, there is strong hybridization between the Bi-6p and the Pd-4d in the whole PDOSs, again verifying the strong interaction between each other.

3.2. NORR catalytic performance of the β-$PdBi_2$ monolayer

Prior to the exploration of the NORR catalytic activity, we first examined the adsorption of the NO reactant on the β-$PdBi_2$ monolayer, which is a pivotal step for affecting or determining the subsequent reduction pathways. To this end, three typical adsorption configurations were considered, namely, N-end, O-end, and side-on patterns (Fig. S3†), on different sites of β-$PdBi_2$, including the top site of Bi, the bridge site of two Bi atoms, and the hollow site of a Bi-based square.

After the fully structural relaxation, we found that NO is the most energetically favorable to be adsorbed on the hollow site of β-$PdBi_2$ *via* the N-end pattern, leading to the formation of four Bi–N bonds with a length of 2.36 Å (Fig. 2a). Moreover, the corresponding adsorption energy (E_{ads}) was determined by: $E_{ads} = E_{*NO} - E_{*} - E_{NO(g)}$, where E_{*NO} and E_{*} represent the DFT energies of β-$PdBi_2$ with and without adsorbed NO molecules, respectively, while $E_{NO(g)}$ is the energy of the isolated NO molecule. According to this definition, the computed E_{ads} value for NO adsorption on β-$PdBi_2$ is −0.92 eV, corresponding to a ΔG of −0.24 eV after taking the contributions of the zero-point and entropy into account (Fig. 2b) and thus suggesting a strong NO chemisorption on β-$PdBi_2$. The chemisorption also elongates the N–O bond length from 1.15 Å in free NO to 1.17 Å in β-$PdBi_2$, indicating that the NO reactant is activated on the β-$PdBi_2$ catalyst surface. Furthermore, the computed PDOSs in Fig. 2c showed that the electronic coupling mainly exists between Bi-6p and NO-2p orbitals. Importantly, β-$PdBi_2$ donates about 0.51 electrons to the adsorbed NO, resulting in the significant accumulation of negative charges (yellow regions in Fig. 2d) on the *NO species, which may promote the subsequent reduction reaction.

In addition to the most stable NO adsorption configuration, we also obtained other several meta-stable configurations: NO is adsorbed on the Bi-atop site *via* the N-end pattern or two possible Bi–Bi bridge sites of β-$PdBi_2$ *via* the side mode (Fig. S4†). The computed E_{ads} values are −0.57, −0.44, and −0.57 eV, respectively, which are less negative than that of on the hollow site of −0.92 eV. Furthermore, as for the O-end pattern, the obtained NO adsorption is even weaker with a considerable small E_{ads} value of −0.27 and −0.04 eV, and the distance between NO and β-$PdBi_2$ is larger than 3.30 Å. As a result, the ΔG values for these meta-stable species are generally positive ranging from 0.11 to 0.64 eV (Fig. 2b), which are

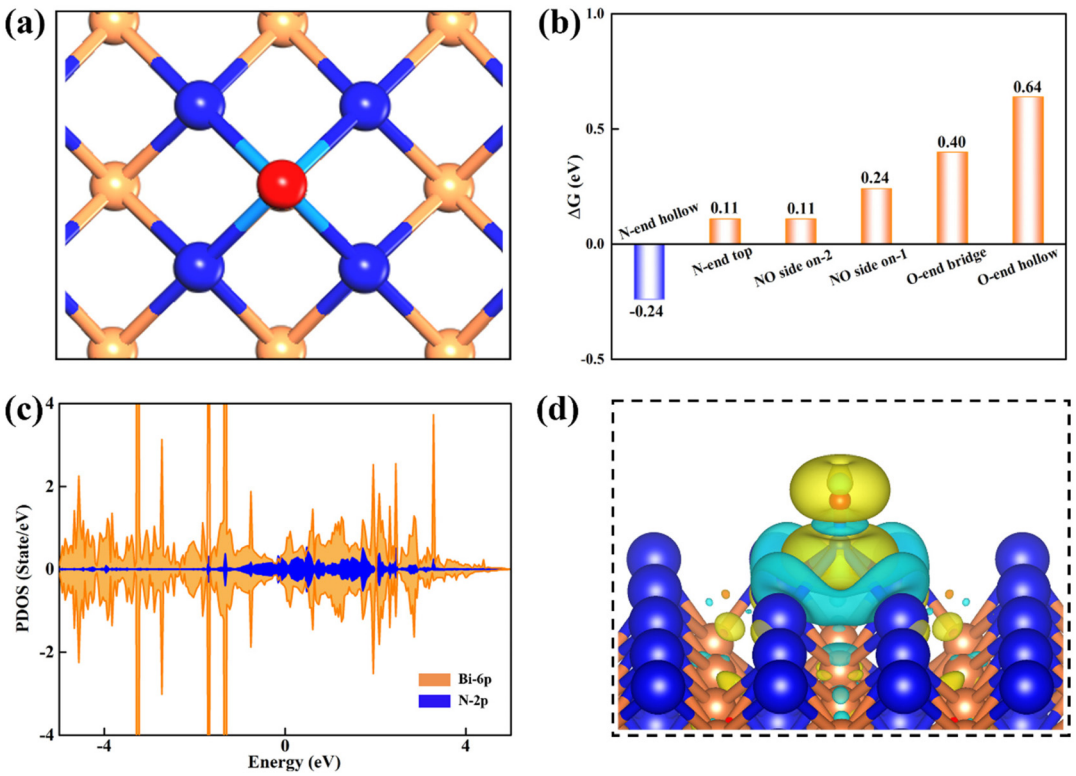

Fig. 2 (a) The optimized configuration, (b) the adsorption free energies (ΔG) for NO adsorption on the β-$PdBi_2$ monolayer in various possible adsorption patterns, (c) the projected density of states (PDOS) and (d) the charge difference density of the β-$PdBi_2$ monolayer with an isovalue of 0.003 e $Å^{-3}$ (before and after NO adsorption). Cyan and yellow bubbles represent positive and negative charges, respectively.

not sufficient to capture the NO molecule on the β-$PdBi_2$ catalyst surface. Thus, the N-end pattern for NO on the hollow site will be mainly focused in the next discussion because this pattern is the most stable.

Initiating from the sufficient activated NO species, we then moved to investigate the catalytic activity on the β-$PdBi_2$ monolayer towards NORR for NH_3 synthesis. In particular, the NORR is a five-step hydrogenation process: $NO + 5H^+ + 5e^- \rightarrow NH_3 + H_2O$, which could involve many possible reaction pathways, such as N-end, O-end, and side-on mechanisms according to previous studies.[29,72–75] As the N-end adsorption configuration was identified as the most stable, we only considered the N-end path as shown in Fig. 3. To this end, we computed the free energy changes of all involved elementary steps in the N-end path for achieving the lowest energy pathway, which requires the least negative applied voltage to make the whole reaction exergonic, namely, the limiting potential (U_L). In Fig. 4, we have presented the free energy diagram and the corresponding reaction intermediates for NORR on the hollow site along the N-end pathway, and more detailed free energy changes of all elementary steps are summarized in Table S1.†

As shown in Fig. 4, two possible reaction intermediates can be generated for the hydrogenation of the N and O sites within the activated *NO species, including *NOH and *NHO. By comparatively computing their ΔG values, we found that the *NHO formation is more energetically favorable due to its smaller ΔG value of 0.35 eV than that of *NOH (ΔG = 0.74 eV). Remarkably, in the formed *NHO species, the N–O bond is further elongated to 1.39 Å. Subsequently, *NHO can be further hydrogenated by reacting with another proton to generate *NHOH or *NH_2O species. The results showed that the formation of *NH_2O is downhill by 0.54 eV, while *NHOH formation is slightly downhill in the free energy profile by 0.04 eV, suggesting the higher feasibility to yield *NH_2O species. The approach of a third proton preferably leads to the dissociation of *NH_2O into *NH_3 and *O. Interestingly, this elementary step is highly exothermic by 1.73 eV, whereas the competitive *NH_2OH formation is endothermic by 0.13 eV. After the release of the NH_3 product, the remaining O atom, which is adsorbed on the Bi–Bi bridge site with a length of 1.34 Å, can be further hydrogenated to *OH and H_2O with ΔG values of −0.62 and −0.64 eV, respectively. Therefore, the potential-determining step during the whole NO electrocatalytic reduction to NH_3 on β-$PdBi_2$ is the hydrogenation of *NO to *NHO due to its maximum ΔG value of 0.35 eV among all elementary steps. Correspondingly, the U_L for NH_3 synthesis from NORR on β-$PdBi_2$ is −0.35 V. As NORR generally proceeds in an aqueous solution, we also examined the solvent effects on the NORR activity of β-$PdBi_2$ by re-computing the free energy profiles of NORR using the implicit solvation model as implemented in VASPsol.[76] As shown in Fig. S5,† we found that the change in the ΔG value of PDS is only 0.02 eV, indicating that the solvent effect has a negligible influence on the NORR activity. A similar small change (0.03 eV) could be also observed for the SOC effect (Fig. S6†). Overall, β-$PdBi_2$ exhibits a superior catalytic activity towards NORR, as its U_L in the PDS is comparable to those of previously reported catalysts (−0.04 to −0.47 V).[26–29,72–77] In particular, the catalytic activity of β-$PdBi_2$ for NORR catalysis is even higher than that of some reported bimetallic catalysts, such as the experimentally reported RuGa catalyst (U_L = −0.49 V),[78] theoretically predicted Cu_2 (U_L = −0.30 V),[79] Mg–Ni@NC (U_L = −0.23 V),[80] and Ga–Cr@NC (U_L = −0.43 V),[80] further testifying the superior per-

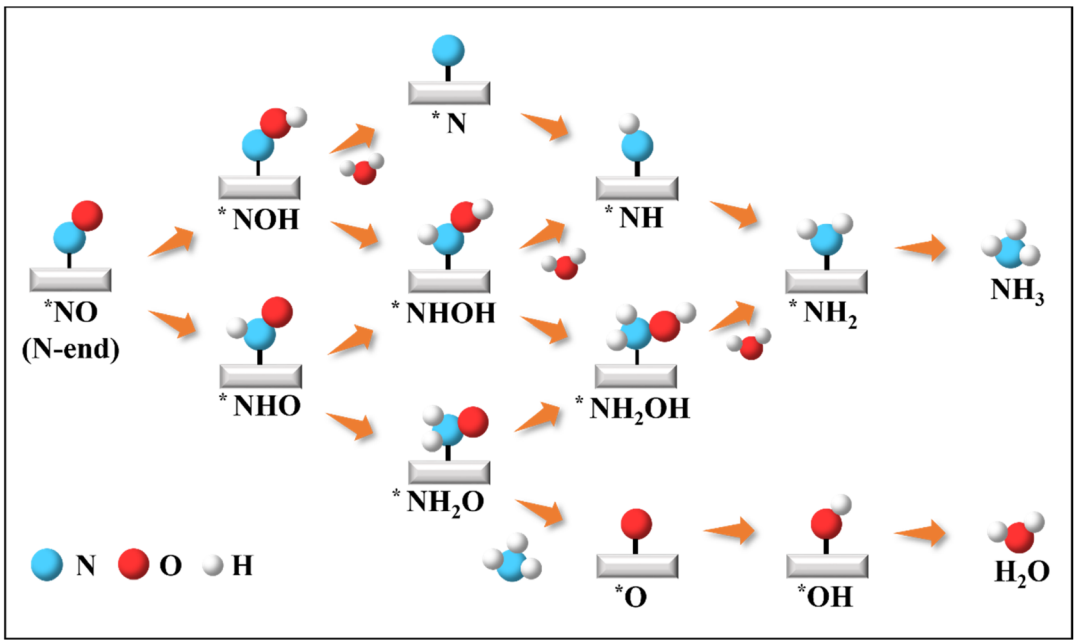

Fig. 3 Schematic depiction of all possible pathways for electrocatalytic NORR to NH_3 along the N-end pathway on the β-$PdBi_2$ monolayer.

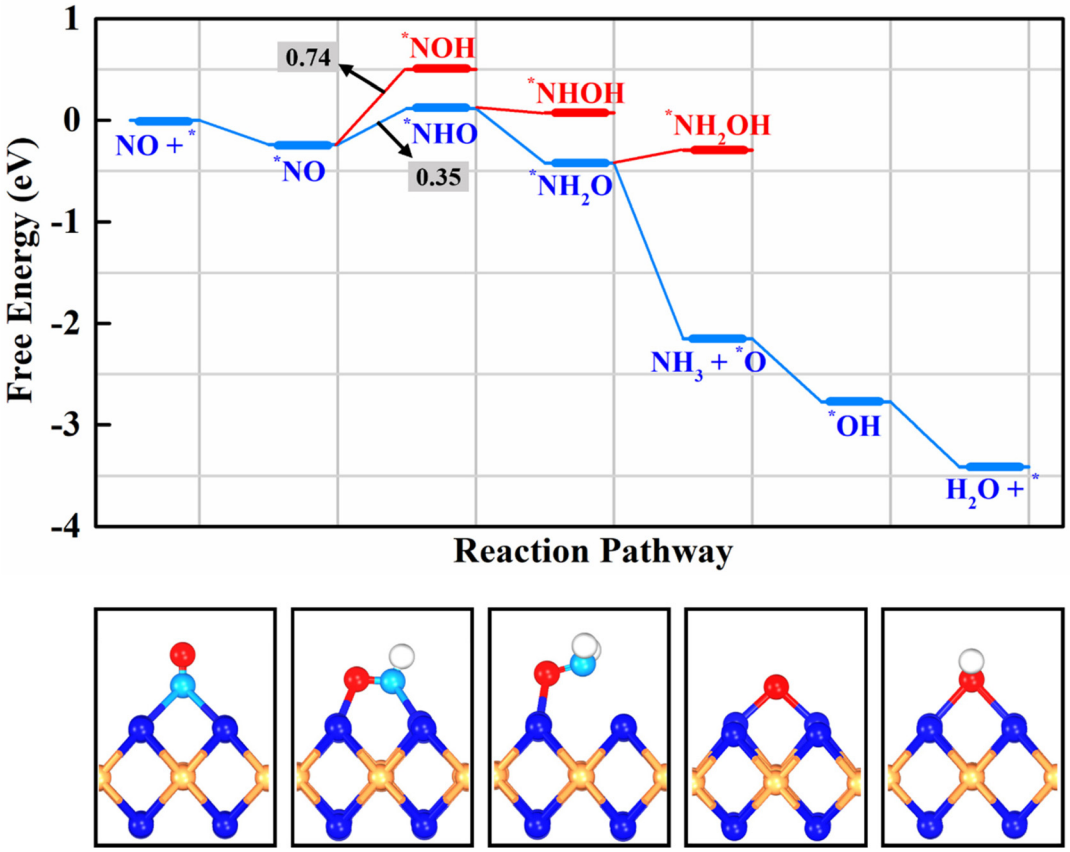

Fig. 4 The energetically most favorable free energy profile for the electroreduction of NO molecules to NH_3 product on the β-$PdBi_2$ monolayer and the involved reaction intermediates. The blue, orange, red, light blue, and white spheres represent the Bi, Pd, O, N, and H atoms, respectively.

formance of the proposed β-$PdBi_2$ for NH_3 synthesis from NORR.

In addition to the NH_3 product at a low NO coverage, N_2 and N_2O are the possible products of NORR at high NO coverage, which can be modulated by controlling the partial pressure according to a recent experimental study reported by Jiao *et al.*[81] To this end, we also examined the feasibility to produce N_2O and N_2 in the NORR process, in which the NO-dimer, *i.e.*, $*N_2O_2$, is a key intermediate. On the β-$PdBi_2$ monolayer, two relatively stable $*N_2O_2$ configurations were obtained *via* the O- and N-end modes with ΔG values of −1.23 and −0.39 eV, respectively (Fig. S7†). Starting from the O-end adsorption configuration, the N_2O product can be generated after two hydrogenation steps, which are downhill in the free energy profile, indicative of the spontaneous N_2O formation (Fig. 5a). We have noted that N_2O adsorption on the β-$PdBi_2$

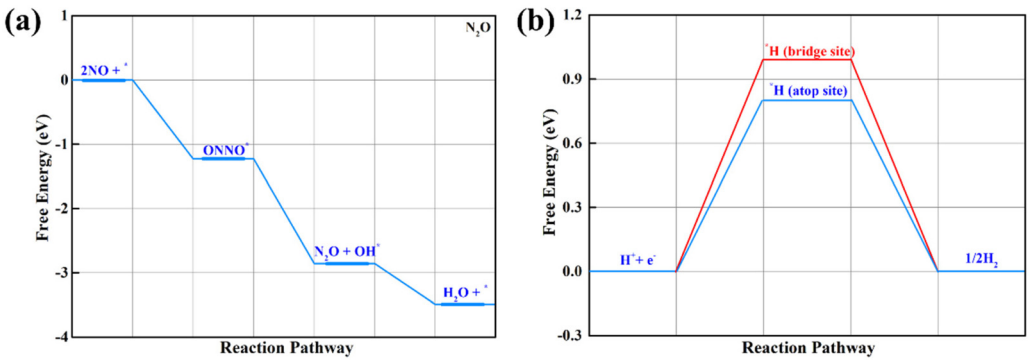

Fig. 5 (a) The energetically most favorable free energy profile for the electroreduction of 2NO molecules to the N_2O product on the β-$PdBi_2$ monolayer and (b) the calculated Gibbs free profile of HER on the β-$PdBi_2$ monolayer.

monolayer is rather weak, enabling its rapid release from the catalyst surface, rather than a further reduction to the N_2 product. Thus, at high NO coverage, N_2O is the main product of NORR on the β-$PdBi_2$ monolayer, which can thus be utilized as a promising catalyst to generate tunable multiproducts by control the NO coverage.[82] Another important question is the competition between NORR and the HER side reaction, which may greatly impact the faradaic efficiency toward NH_3 synthesis. After considering various initial adsorption sites, including atop, bridge, and hollow sites, we found that the *H adsorption on the Bi–Bi bridge site and Bi atop site is stable, and the computed ΔG values are 0.99 and 0.80 eV, respectively, as shown in Fig. 5b, which is much larger than that of the PDS in NORR (0.35 eV), implying its overwhelming suppressing effect on HER and thus guaranteeing the high NORR selectivity.

3.3. Effect of strain on the NO-to-NH_3 catalytic activity

Strain engineering has been widely reported to be a powerful strategy to tailor the reactivity of eletrocatalysts for achieving outstanding performance.[83–85] Thus, the external biaxial tensile strain was imposed on β-$PdBi_2$ (Fig. 6a), which can be realized by direct stretching or using a pre-stretched substrate in the experiment. Note that the strain range is from 1% to 7% with a step of 1%. Our AIMD simulations showed that the structural integrity of β-$PdBi_2$ can be well maintained under a 7% tensile strain (Fig. S8†), indicating its rather high thermodynamic stability. Moreover, we re-computed the free energy diagrams of the NO-to-NH_3 process, which was plotted as a function of the external tensile strain (Fig. 6b). Our results showed that the binding strength of NO will be weakened with the increase of strain (E_{ads} for NO decreases from −0.92 eV to −0.61 eV at a 7% strain). Moreover, the PDS is unchanged with the variation of strain, which always occurs in the first hydrogenation step (*NO + H^+ + e^- → *NHO). Interestingly, the computed ΔG value of this step decreases gradually, implying the decrease of the limiting potential with the enhancement of the tensile strain. As a result, the NO reduction on β-$PdBi_2$ exhibits the highest catalytic activity with a limiting potential of −0.09 V after applying 7% tensile strain (Fig. 6c), suggesting that the strain engineering can greatly enhance the NORR catalytic activity of β-$PdBi_2$ for NH_3 synthesis. Notably, under the tensile strain of 7%, the competing HER reaction is still greatly suppressed due to its larger energy input (0.64 eV, Fig. S9†), suggesting that the high NORR selectivity is unchanged by the tensile strain.

As discussed above, the NORR activity of β-$PdBi_2$ at different tensile strains is highly dependent on the binding strength of *NO: the adsorption strength of *NO should be as small as possible, but large enough to prevent NO desorption, which is well consistent with the famous Sabatier principle. Thus, to gain a vivid insight into the strain effect on the NORR activity of the β-$PdBi_2$ monolayer, it is essential to analyze the bonding nature of the adsorbed *NO species. Hence, we com-

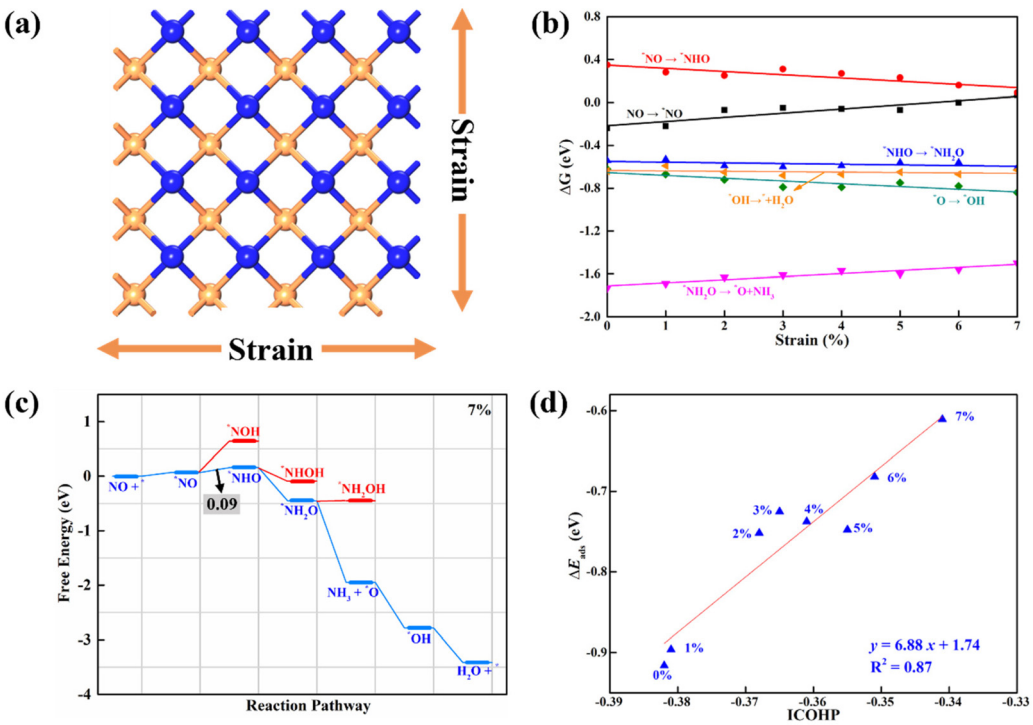

Fig. 6 (a) Schematic of the β-$PdBi_2$ monolayer under biaxial tensile strain; (b) the relationship of ΔG with the strain; (c) the energetically most favorable free energy profile for the electroreduction of NO molecules to the NH_3 product on the β-$PdBi_2$ monolayer after applying 7% tensile strain and (d) the correlation of the adsorption energy (ΔE_{ads}) of *NO species with the integrated crystal orbital Hamilton population (ICOHP).

puted the projected crystal orbital Hamilton population (pCOHP) of the formed Bi–N bonds between *NO and the β-$PdBi_2$ monolayer. As shown in Fig. S10,† the regions in the Bi–N antibonding states around the Fermi level increase with the increase of tensile strain, indicative of a weakened binding strength of the *NO species on the strained β-$PdBi_2$ monolayer. The weakened Bi–N bond was further testified using a less negative integrated crystal orbital Hamilton population (ICOHP). More importantly, there is a good linear relationship between ICOHP and E_{ads} of *NO (Fig. 6d), which well accounts for the role of the external tensile strain in determining the occupancy of the Bi–N bonding/antibonding orbital populations.

3.4. pH-Dependent NORR activity

Although the CHE model has been successfully employed to rapidly screen out promising electrocatalysts and to well explain the underlying reaction mechanism, the pH-dependent activity of a given electrocatalyst can not be accurately reflected due to the limitations of a simple metal/vacuum model at zero charge to represent a charged electrochemical interface normally operating at constant potential conditions. Thus, we employed the constant-potential method (CPM)[86–90] to examine the effects of pH values on the NORR catalytic activity of a 2D β-$PdBi_2$ monolayer. The computed total energies of bare β-$PdBi_2$ and its surface with adsorbed NORR intermediates (*NO, *NHO, *NH_2O, *O, and *OH) as a function of the applied electrode potential (standard hydrogen electrode, SHE) are shown in Fig. 7a. Interestingly, we found that all energy-potential points well fit a quadratic relation, and the fitted data are summarized in Table S2.† The computed E_{ads} values of the five reaction intermediates with respect to the applied potential are presented in Fig. 7b. Clearly, the adsorption energy of *NO is highly dependent on the applied potential, which would affect the limiting potential under different applied potentials and pH values. Furthermore, we plotted the pH-dependent and potential-dependent contour of adsorption energies of *NO on β-$PdBi_2$ (Fig. 7c). The results indicated that the adsorption strength of *NO on β-$PdBi_2$ increases as the pH increases or the applied potential decreases. For example, the E_{ads} of *NO is −0.42 eV at pH = 1, while it can be increased to −0.83 eV at pH = 13. Thus, the acidic environment makes the *NO activation more difficult due to its weak capability to activate the NO reactant, which may explain the pH-dependent NORR activity of the β-$PdBi_2$ monolayer. More importantly, we found that this system will exhibit the highest catalytic activity at a pH of 7.92 with the limiting potential of −0.23 V *vs.* reverse hydrogen electrode (RHE) due to its optimal *NO adsorption energy of −0.68 eV. The corresponding free energy profile is presented in Fig. 7d.

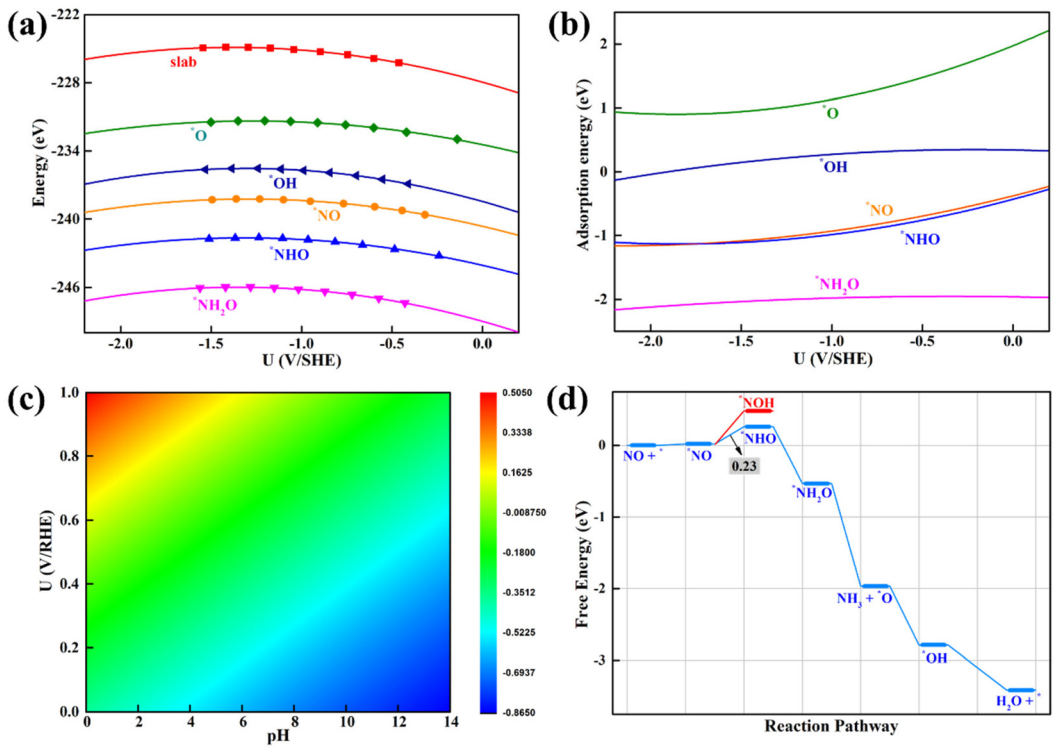

Fig. 7 (a) Computed energies of the β-$PdBi_2$ monolayer and the corresponding reaction intermediates as a function of the applied electrode potential. (b) Adsorption energies of *NO, *NHO, *NH_2O, *O, and *OH as a function of the applied electrode potential. (c) pH-Dependent and potential-dependent contour plot of adsorption energies of *NO on the β-$PdBi_2$ monolayer. (d) The free energy profile for NO-to-NH_3 electrocatalytic reduction on the β-$PdBi_2$ monolayer in pH = 7.92.

4. Conclusions

In summary, by performing comprehensive DFT computations, we explored the catalytic performance of the experimentally available β-$PdBi_2$ monolayer for the NO electrocatalytic reduction to NH_3. Interestingly, our results revealed that the β-$PdBi_2$ monolayer with high stability and inherent metallicity exhibits a superior NOER catalytic performance for NH_3 synthesis with a low limiting potential (−0.35 V) and the overwhelming suppressing effect on HER. Particularly, applying a 7% tensile strain can effectively optimize the NO adsorption strength to further enhance the NOER catalytic activity of the β-$PdBi_2$ monolayer. More importantly, based on the constant-potential method, we found that the alkaline conditions with a pH of 7.92 are also beneficial for boosting the effective NO conversion to NH_3. Our findings not only present an ideal candidate for NO-to-NH_3 electrolysis, but also offer promising strategies to enhance the NORR catalytic activity, which would inspire more experimental and theoretical studies to explore the potential of main-group metal materials in electrocatalysis.

Conflicts of interest

The authors declare no competing financial interest.

Acknowledgements

This work was financially supported by the Natural Science Foundation of Heilongjiang Province of China (TD2020B001) and the Natural Science Funds for Distinguished Young Scholar of Heilongjiang Province (no. JC2018004).

References

1 J. W. Erisman, M. A. Sutton, J. Galloway, Z. Klimont and W. Winiwarter, How a century of ammonia synthesis changed the world, *Nat. Geosci.*, 2008, **1**, 636–639.
2 J. N. Galloway, A. R. Townsend, J. W. Erisman, M. Bekunda, Z. Cai, J. R. Freney, L. A. Martinelli, S. P. Seitzinger and M. A. Sutton, Transformation of the Nitrogen Cycle: Recent Trends, Questions, and Potential Solutions, *Science*, 2008, **320**, 889–892.
3 J. Lim, C. A. Fernández, S. W. Lee and M. C. Hatzell, Ammonia and Nitric Acid Demands for Fertilizer Use in 2050, *ACS Energy Lett.*, 2021, **6**, 3676–3685.
4 G. Qing, R. Ghazfar, S. T. Jackowski, F. Habibzadeh, M. M. Ashtiani, C.-P. Chen, M. R. Smith, III and T. W. Hamann, Recent Advances and Challenges of Electrocatalytic N_2 Reduction to Ammonia, *Chem. Rev.*, 2020, **120**, 5437–5516.
5 S. Mukherjee, S. V. Devaguptapu, A. Sviripa, C. R. F. Lund and G. Wu, Low-temperature ammonia decomposition catalysts for hydrogen generation, *Appl. Catal., B*, 2018, **226**, 162–181.
6 H. Ishaq, I. Dincer and C. Crawford, A review on hydrogen production and utilization: Challenges and opportunities, *Int. J. Hydrogen Energy*, 2022, **47**, 26238–26264.
7 C. Smith, A. K. Hill and L. Torrente-Murciano, Current and future role of Haber–Bosch ammonia in a carbon-free energy landscape, *Energy Environ. Sci.*, 2020, **13**, 331–344.
8 J. Guo and P. Chen, Ammonia history in the making, *Nat. Catal.*, 2021, **4**, 734–735.
9 S. D. Minteer, P. Christopher and S. Linic, Recent Developments in Nitrogen Reduction Catalysts: A Virtual Issue, *ACS Energy Lett.*, 2019, **4**, 163–166.
10 A. J. Martín, T. Shinagawa and J. Pérez-Ramírez, Electrocatalytic Reduction of Nitrogen: From Haber-Bosch to Ammonia Artificial Leaf, *Chem*, 2019, **5**, 263–283.
11 C. Guo, J. Ran, A. Vasileff and S.-Z. Qiao, Rational design of electrocatalysts and photo(electro)catalysts for nitrogen reduction to ammonia (NH_3) under ambient conditions, *Energy Environ. Sci.*, 2018, **11**, 45–56.
12 F. Jiao and B. Xu, Electrochemical Ammonia Synthesis and Ammonia Fuel Cells, *Adv. Mater.*, 2019, **31**, 1805173.
13 H. Liu, Ammonia synthesis catalyst 100 years: Practice, enlightenment and challenge, *Chin. J. Catal.*, 2014, **35**, 1619–1640.
14 Q. Wang, J. Guo and P. Chen, Recent progress towards mild-condition ammonia synthesis, *J. Energy Chem.*, 2019, **36**, 25–36.
15 G.-F. Chen, S. Ren, L. Zhang, H. Cheng, Y. Luo, K. Zhu, L.-X. Ding and H. Wang, Advances in Electrocatalytic N_2 Reduction-Strategies to Tackle the Selectivity Challenge, *Small Methods*, 2019, **3**, 1800337.
16 A. R. Singh, B. A. Rohr, J. A. Schwalbe, M. Cargnello, K. Chan, T. F. Jaramillo, I. Chorkendorff and J. K. Norskov, Electrochemical Ammonia Synthesis – The Selectivity Challenge, *ACS Catal.*, 2017, **7**, 706–709.
17 C. J. M. van der Ham, M. T. M. Koper and D. G. H. Hetterscheid, Challenges in reduction of dinitrogen by proton and electron transfer, *Chem. Soc. Rev.*, 2014, **43**, 5183–5191.
18 Y. Yao, J. Wang, U. B. Shahid, M. Gu, H. Wang, H. Li and M. Shao, Electrochemical Synthesis of Ammonia from Nitrogen Under Mild Conditions: Current Status and Challenges, *Electrochem. Energy Rev.*, 2020, **3**, 239–270.
19 J. Long, S. Chen, Y. Zhang, C. Guo, X. Fu, D. Deng and J. Xiao, Direct Electrochemical Ammonia Synthesis from Nitric Oxide, *Angew. Chem., Int. Ed.*, 2020, **59**, 9711–9718.
20 T. Mou, J. Long, T. Frauenheim and J. Xiao, Advances in Electrochemical Ammonia Synthesis Beyond the Use of Nitrogen Gas as a Source, *ChemPlusChem*, 2021, **86**, 1211–1224.
21 A. Clayborne, H.-J. Chun, R. B. Rankin and J. Greeley, Elucidation of Pathways for NO Electroreduction on Pt(111) from First Principles, *Angew. Chem., Int. Ed.*, 2015, **54**, 8255–8258.
22 T.-M. Chen, W. G. Kuschner, J. Gokhale and S. Shofer, Outdoor Air Pollution: Nitrogen Dioxide, Sulfur Dioxide,

and Carbon Monoxide Health Effects, *Am. J. Med. Sci.*, 2007, **333**, 249–256.

23 M. Kampa and E. Castanas, Human health effects of air pollution, *Environ. Pollut.*, 2008, **151**, 362–367.

24 A. Larkin, J. A. Geddes, R. V. Martin, Q. Xiao, Y. Liu, J. D. Marshall, M. Brauer and P. Hystad, Global Land Use Regression Model for Nitrogen Dioxide Air Pollution, *Environ. Sci. Technol.*, 2017, **51**, 6957–6964.

25 C. He, R. Sun, L. Fu, J. Huo, C. Zhao, X. Li, Y. Song and S. Wang, Defect engineering for high-selection-performance of NO reduction to NH_3 over CeO_2 (111) surface: A DFT study, *Chin. Chem. Lett.*, 2022, **33**, 527–532.

26 H. Niu, Z. Zhang, X. Wang, X. Wan, C. Kuai and Y. Guo, A Feasible Strategy for Identifying Single-Atom Catalysts Toward Electrochemical NO-to-NH_3 Conversion, *Small*, 2021, **17**, 2102396.

27 Z. Ren, H. Zhang, S. Wang, B. Huang, Y. Dai and W. Wei, Nitric oxide reduction reaction for efficient ammonia synthesis on topological nodal-line semimetal Cu_2Si monolayer, *J. Mater. Chem. A*, 2022, **10**, 8568–8577.

28 Y. Zang, Q. Wu, S. Wang, B. Huang, Y. Dai and Y. Ma, High-Throughput Screening of Efficient Biatom Catalysts Based on Monolayer Carbon Nitride for the Nitric Oxide Reduction Reaction, *J. Phys. Chem. Lett.*, 2022, **13**, 527–535.

29 Q. Wu, H. Wang, S. Shen, B. Huang, Y. Dai and Y. Ma, Efficient nitric oxide reduction to ammonia on a metal-free electrocatalyst, *J. Mater. Chem. A*, 2021, **9**, 5434–5441.

30 Q. Wu, W. Wei, X. Lv, Y. Wang, B. Huang and Y. Dai, Cu@g-C_3N_4: An Efficient Single-Atom Electrocatalyst for NO Electrochemical Reduction with Suppressed Hydrogen Evolution, *J. Phys. Chem. C*, 2019, **123**, 31043–31049.

31 I. Katsounaros, M. C. Figueiredo, X. Chen, F. Calle-Vallejo and M. T. M. Koper, Structure- and Coverage-Sensitive Mechanism of NO Reduction on Platinum Electrodes, *ACS Catal.*, 2017, **7**, 4660–4667.

32 Z. Wang, J. Zhao, J. Wang, C. R. Cabrera and Z. Chen, A Co–N_4 moiety embedded into graphene as an efficient single-atom-catalyst for NO electrochemical reduction: a computational study, *J. Mater. Chem. A*, 2018, **6**, 7547–7556.

33 J. Long, C. Guo, X. Fu, H. Jing, G. Qin, H. Li and J. Xiao, Unveiling Potential Dependence in NO Electroreduction to Ammonia, *J. Phys. Chem. Lett.*, 2021, **12**, 6988–6995.

34 L. Zhang, J. Liang, Y. Wang, T. Mou, Y. Lin, L. Yue, T. Li, Q. Liu, Y. Luo, N. Li, B. Tang, Y. Liu, S. Gao, A. A. Alshehri, X. Guo, D. Ma and X. Sun, High-Performance Electrochemical NO Reduction into NH_3 by MoS_2 Nanosheet, *Angew. Chem., Int. Ed.*, 2021, **60**, 25263–25268.

35 T. Mou, J. Liang, Z. Ma, L. Zhang, Y. Lin, T. Li, Q. Liu, Y. Luo, Y. Liu, S. Gao, H. Zhao, A. M. Asiri, D. Ma and X. Sun, High-efficiency electrohydrogenation of nitric oxide to ammonia on a Ni_2P nanoarray under ambient conditions, *J. Mater. Chem. A*, 2021, **9**, 24268–24275.

36 D. Kim, D. Shin, J. Heo, H. Lim, J.-A. Lim, H. M. Jeong, B.-S. Kim, I. Heo, I. Oh, B. Lee, M. Sharma, H. Lim, H. Kim and Y. Kwon, Unveiling Electrode–Electrolyte Design-Based NO Reduction for NH_3 Synthesis, *ACS Energy Lett.*, 2020, **5**, 3647–3656.

37 Y. Guan, M. Liu, X. Rao, Y. Liu and J. Zhang, Electrochemical reduction of carbon dioxide (CO_2): bismuth-based electrocatalysts, *J. Mater. Chem. A*, 2021, **9**, 13770–13803.

38 D. Xia, H. Yu, H. Xie, P. Huang, R. Menzel, M. M. Titirici and G. Chai, Recent progress of Bi-based electrocatalysts for electrocatalytic CO_2 reduction, *Nanoscale*, 2022, **14**, 7957–7973.

39 K. Xu, L. Wang, X. Xu, S. X. Dou, W. Hao and Y. Du, Two dimensional bismuth-based layered materials for energy-related applications, *Energy Storage Mater.*, 2019, **19**, 446–463.

40 C. Yang, J. Chai, Z. Wang, Y. Xing, J. Peng and Q. Yan, Recent Progress on Bismuth-based Nanomaterials for Electrocatalytic Carbon Dioxide Reduction, *Chem. Res. Chin. Univ.*, 2020, **36**, 410–419.

41 W. P. Utomo, M. K. H. Leung, Z. Yin, H. Wu and Y. H. Ng, Advancement of Bismuth-Based Materials for Electrocatalytic and Photo(electro)catalytic Ammonia Synthesis, *Adv. Funct. Mater.*, 2022, **32**, 2106713.

42 X. Xue, R. Chen, H. Chen, Y. Hu, Q. Ding, Z. Liu, L. Ma, G. Zhu, W. Zhang, Q. Yu, J. Liu, J. Ma and Z. Jin, Oxygen Vacancy Engineering Promoted Photocatalytic Ammonia Synthesis on Ultrathin Two-Dimensional Bismuth Oxybromide Nanosheets, *Nano Lett.*, 2018, **18**, 7372–7377.

43 Y. Sun, Z. Deng, X.-M. Song, H. Li, Z. Huang, Q. Zhao, D. Feng, W. Zhang, Z. Liu and T. Ma, Bismuth-Based Free-Standing Electrodes for Ambient-Condition Ammonia Production in Neutral Media, *Nano-Micro Lett.*, 2020, **12**, 133.

44 D. Yao, C. Tang, L. Li, B. Xia, A. Vasileff, H. Jin, Y. Zhang and S.-Z. Qiao, In Situ Fragmented Bismuth Nanoparticles for Electrocatalytic Nitrogen Reduction, *Adv. Energy Mater.*, 2020, **10**, 2001289.

45 L. Li, C. Tang, B. Xia, H. Jin, Y. Zheng and S.-Z. Qiao, Two-Dimensional Mosaic Bismuth Nanosheets for Highly Selective Ambient Electrocatalytic Nitrogen Reduction, *ACS Catal.*, 2019, **9**, 2902–2908.

46 J. Greeley, T. F. Jaramillo, J. Bonde, I. Chorkendorff and J. K. Nørskov, Computational high-throughput screening of electrocatalytic materials for hydrogen evolution, *Nat. Mater.*, 2006, **5**, 909–913.

47 S. Kim, W. J. Dong, S. Gim, W. Sohn, J. Y. Park, C. J. Yoo, H. W. Jang and J.-L. Lee, Shape-controlled bismuth nanoflakes as highly selective catalysts for electrochemical carbon dioxide reduction to formate, *Nano Energy*, 2017, **39**, 44–52.

48 P. Lu, D. Gao, H. He, Q. Wang, Z. Liu, S. Dipazir, M. Yuan, W. Zu and G. Zhang, Facile synthesis of a bismuth nanostructure with enhanced selectivity for electrochemical conversion of CO_2 to formate, *Nanoscale*, 2019, **11**, 7805–7812.

49 X. Chia and M. Pumera, Characteristics and performance of two-dimensional materials for electrocatalysis, *Nat. Catal.*, 2018, **1**, 909–921.

50 X. Zhang, A. Chen, L. Chen and Z. Zhou, 2D Materials Bridging Experiments and Computations for Electro/Photocatalysis, *Adv. Energy Mater.*, 2022, **12**, 2003841.
51 Y. Zhang, X. Zhang, Y. Ling, F. Li, A. M. Bond and J. Zhang, Controllable Synthesis of Few-Layer Bismuth Subcarbonate by Electrochemical Exfoliation for Enhanced CO_2 Reduction Performance, *Angew. Chem., Int. Ed.*, 2018, **57**, 13283–13287.
52 Y. Wan, H. Zhou, M. Zheng, Z.-H. Huang, F. Kang, J. Li and R. Lv, Oxidation State Modulation of Bismuth for Efficient Electrocatalytic Nitrogen Reduction to Ammonia, *Adv. Funct. Mater.*, 2021, **31**, 2100300.
53 N. V. Denisov, A. V. Matetskiy, A. V. Tupkalo, A. V. Zotov and A. A. Saranin, Growth of layered superconductor β-$PdBi_2$ films using molecular beam epitaxy, *Appl. Surf. Sci.*, 2017, **401**, 142–145.
54 G. Kresse and J. Hafner, Ab initio molecular dynamics for liquid metals, *Phys. Rev. B: Condens. Matter Mater. Phys.*, 1993, **47**, 558–561.
55 G. Kresse and J. Furthmüller, Efficient iterative schemes for ab initio total-energy calculations using a plane-wave basis set, *Phys. Rev. B: Condens. Matter Mater. Phys.*, 1996, **54**, 11169–11186.
56 P. E. Blochl, Projector augmented-wave method, *Phys. Rev. B: Condens. Matter Mater. Phys.*, 1994, **50**, 17953–17979.
57 G. Kresse and D. Joubert, From ultrasoft pseudopotentials to the projector augmented-wave method, *Phys. Rev. B: Condens. Matter Mater. Phys.*, 1999, **59**, 1758–1775.
58 J. P. Perdew, K. Burke and M. Ernzerhof, Generalized gradient approximation made simple, *Phys. Rev. Lett.*, 1996, **77**, 3865–3868.
59 S. Grimme, Semiempirical GGA-type density functional constructed with a long-range dispersion correction, *J. Comput. Chem.*, 2006, **27**, 1787–1799.
60 J. Heyd, G. E. Scuseria and M. Ernzerhof, Hybrid functionals based on a screened Coulomb potential, *J. Chem. Phys.*, 2003, **118**, 8207–8215.
61 J. Heyd, G. E. Scuseria and M. Ernzerhof, Hybrid functionals based on a screened Coulomb potential, *J. Chem. Phys.*, 2006, **124**, 219906.
62 G. J. Martyna, M. L. Klein and M. Tuckerman, Nose-Hoover chains: The canonical ensemble via continuous dynamics, *J. Chem. Phys.*, 1992, **97**, 2635–2643.
63 J. K. Norskov, J. Rossmeisl, A. Logadottir, L. Lindqvist, J. R. Kitchin, T. Bligaard and H. Jonsson, Origin of the overpotential for oxygen reduction at a fuel-cell cathode, *J. Phys. Chem. B*, 2004, **108**, 17886–17892.
64 A. A. Peterson, F. Abild-Pedersen, F. Studt, J. Rossmeisl and J. K. Norskov, How copper catalyzes the electroreduction of carbon dioxide into hydrocarbon fuels, *Energy Environ. Sci.*, 2010, **3**, 1311–1315.
65 X. Zhu, Y. Wang, Y. Jing, T. Heine and Y. Li, β-$PdBi_2$ monolayer: two-dimensional topological metal with superior catalytic activity for carbon dioxide electroreduction to formic acid, *Mater. Today Adv.*, 2020, **8**, 100091.
66 P.-F. Liu, J. Li, X.-H. Tu, H. Yin, B. Sa, J. Zhang, D. J. Singh and B.-T. Wang, Prediction of superconductivity and topological aspects in single-layer β-Bi_2Pd, *Phys. Rev. B*, 2020, **102**, 155406.
67 M. Sakano, K. Okawa, M. Kanou, H. Sanjo, T. Okuda, T. Sasagawa and K. Ishizaka, Topologically protected surface states in a centrosymmetric superconductor β-$PdBi_2$, *Nat. Commun.*, 2015, **6**, 8595.
68 L.-M. Yang, V. Bačić, I. A. Popov, A. I. Boldyrev, T. Heine, T. Frauenheim and E. Ganz, Two-Dimensional Cu_2Si Monolayer with Planar Hexacoordinate Copper and Silicon Bonding, *J. Am. Chem. Soc.*, 2015, **137**, 2757–2762.
69 J. Jia, Z. Chen, Y. Liu, Y. Li and J. Zhao, RuN_2 Monolayer: A Highly Efficient Electrocatalyst for Oxygen Reduction Reaction, *ACS Appl. Mater. Interfaces*, 2020, **12**, 54517–54523.
70 J. Jia, H. Zhang, Z. Wang, J. Zhao and Z. Zhou, A Cu_2B_2 monolayer with planar hypercoordinate motifs: an efficient catalyst for CO electroreduction to ethanol, *J. Mater. Chem. A*, 2020, **8**, 9607–9615.
71 X. Zhu, X. Zhou, Y. Jing and Y. Li, Electrochemical synthesis of urea on MBenes, *Nat. Commun.*, 2021, **12**, 4080.
72 Y. Xiao and C. Shen, Transition-Metal Borides (MBenes) as New High-Efficiency Catalysts for Nitric Oxide Electroreduction to Ammonia by a High-Throughput Approach, *Small*, 2021, **17**, 2100776.
73 Z. Lang, J. Miao, H. Tan, Z. Su, Y. Li and Z. Zheng, Element table of TM-substituted polyoxotungstates for direct electrocatalytic reduction of nitric oxide to ammonia: a DFT guideline for experiments, *Inorg. Chem. Front.*, 2020, **7**, 4507–4516.
74 Q. Zhou, F. Gong, Y. Xie, D. Xia, Z. Hu, S. Wang, L. Liu and R. Xiao, A general strategy for designing metal-free catalysts for highly-efficient nitric oxide reduction to ammonia, *Fuel*, 2022, **310**, 122442.
75 M. Tursun and C. Wu, Single Transition Metal Atoms Anchored on Defective MoS_2 Monolayers for the Electrocatalytic Reduction of Nitric Oxide into Ammonia and Hydroxylamine, *Inorg. Chem.*, 2022, **61**, 17448–17458.
76 K. Mathew, R. Sundararaman, K. Letchworth-Weaver, T. A. Arias and R. G. Hennig, Implicit solvation model for density-functional study of nanocrystal surfaces and reaction pathways, *J. Chem. Phys.*, 2014, **140**, 084106.
77 T. Tong, Y. Linghu, G. Wu, C. Wang and C. Wu, Nitric oxide electrochemical reduction reaction on transition metal-doped $MoSi_2N_4$ monolayers, *Phys. Chem. Chem. Phys.*, 2022, **24**, 18943–18951.
78 H. Zhang, Y. Li, C. Cheng, J. Zhou, P. Yin, H. Wu, Z. Liang, J. Zhang, Q. Yun, A. Wang, L. Zhu, B. Zhang, W. Cao, X. Meng, J. Xia, Y. Yu and Q. Lu, Isolated Electron-Rich Ruthenium Atoms in Intermetallic Compounds for Boosting Electrochemical Nitric Oxide Reduction to Ammonia, *Angew. Chem., Int. Ed.*, 2023, **62**, e202213351.
79 P. Lv, D. Wu, B. He, X. Li, R. Zhu, G. Tang, Z. Lu, D. Ma and Y. Jia, An efficient screening strategy towards multifunctional catalysts for the simultaneous electroreduction

of NO^{3-}, NO^{2-} and NO to NH_3, *J. Mater. Chem. A*, 2022, **10**, 9707–9716.

80 Y. Zang, Q. Wu, S. Wang, B. Huang, Y. Dai and Y. Ma, Coupling a Main-Group Metal with a Transition Metal to Create Biatom Catalysts for Nitric Oxide Reduction, *Phys. Rev. Appl.*, 2023, **19**, 024003.

81 B. H. Ko, B. Hasa, H. Shin, Y. Zhao and F. Jiao, Electrochemical Reduction of Gaseous Nitrogen Oxides on Transition Metals at Ambient Conditions, *J. Am. Chem. Soc.*, 2022, **144**, 1258–1266.

82 Y. Li, C. Cheng, S. Han, Y. Huang, X. Du, B. Zhang and Y. Yu, Electrocatalytic Reduction of Low-Concentration Nitric Oxide into Ammonia over Ru Nanosheets, *ACS Energy Lett.*, 2022, **7**, 1187–1194.

83 L. Wang, Z. Zeng, W. Gao, T. Maxson, D. Raciti, M. Giroux, X. Pan, C. Wang and J. Greeley, Tunable intrinsic strain in two-dimensional transition metal electrocatalysts, *Science*, 2019, **363**, 870–874.

84 Z. Xia and S. Guo, Strain engineering of metal-based nanomaterials for energy electrocatalysis, *Chem. Soc. Rev.*, 2019, **48**, 3265–3278.

85 X. Yang, Y. Wang, X. Tong and N. Yang, Strain Engineering in Electrocatalysts: Fundamentals, Progress, and Perspectives, *Adv. Energy Mater.*, 2022, **12**, 2102261.

86 X. Hu, S. Chen, L. Chen, Y. Tian, S. Yao, Z. Lu, X. Zhang and Z. Zhou, What is the Real Origin of the Activity of Fe–N–C Electrocatalysts in the O_2 Reduction Reaction? Critical Roles of Coordinating Pyrrolic N and Axially Adsorbing Species, *J. Am. Chem. Soc.*, 2022, **144**(39), 18144–18152.

87 Z. Duan and G. Henkelman, Theoretical Resolution of the Exceptional Oxygen Reduction Activity of Au(100) in Alkaline Media, *ACS Catal.*, 2019, **9**, 5567–5573.

88 Z. Duan and G. Henkelman, Identification of Active Sites of Pure and Nitrogen-Doped Carbon Materials for Oxygen Reduction Reaction Using Constant-Potential Calculations, *J. Phys. Chem. C*, 2020, **124**, 12016–12023.

89 Z. Duan and G. Henkelman, Surface Charge and Electrostatic Spin Crossover Effects in CoN_4 Electrocatalysts, *ACS Catal.*, 2020, **10**, 12148–12155.

90 Z. Duan and G. Henkelman, Atomic-Scale Mechanisms of Electrochemical Pt Dissolution, *ACS Catal.*, 2021, **11**, 14439–14447.

